

This content has been downloaded from IOPscience. Please scroll down to see the full text.

Download details:

IP Address: 3.17.162.247

This content was downloaded on 27/04/2024 at 07:42

Please note that [terms and conditions apply](#).

You may also like:

[Neurological Disorders and Imaging Physics, Volume 1](#)

[Advances in Drug Delivery Systems for Healthcare](#)

[Testing the quality of images for permanent magnet desktop MRI systems using specially designed phantoms](#)

Jianfeng Qiu, Guozhu Wang, Jiao Min et al.

[Noise-residue learning convolutional network model for magnetic resonance image enhancement](#)

Ram Singh and Lakhwinder Kaur

[FPGA-based RF interference reduction techniques for simultaneous PET–MRI](#)

P Gebhardt, J Wehner, B Weissler et al.

[SQUIDS in biomagnetism: a roadmap towards improved healthcare](#)

Rainer Körber, Jan-Hendrik Storm, Hugh Seton et al.

[Development of an MRI-compatible digital SiPM detector stack for simultaneous PET/MRI](#)

Peter M Düppenbecker, Bjoern Weissler, Pierre Gebhardt et al.

# The Physics and Mathematics of MRI

**Richard Ansorge and Martin Graves**

---

## Chapter 1

### The basics

In this chapter we introduce magnetic resonance imaging (MRI), starting with a brief history and then explaining the physics of proton spin and the way ensembles of spins relax back to equilibrium after a perturbation thereby generating the signals that are the basis for both nuclear magnetic resonance (NMR) and MRI. Finally, we introduce the methods used to obtain position dependent signals—or images.

#### 1.1 A brief history of MRI

There are arguably three strands to the story of MRI: firstly, there is the discovery and basic understanding of nuclear spin, particularly that of the proton. Secondly, there is the development of methods to exploit excitation of nuclear spins for spectroscopy (NMR) and later imaging (MRI). Finally, there is the development of the very high field superconducting magnets that are necessary for real world practical applications.

Much (but not all) of the story can be found in table 1.1 of Nobel prizes awarded for relevant work.

##### 1.1.1 Spin and magnetic moments

The iconic Stern–Gerlach experiment performed in 1922 (Gerlach and Stern 1922a, 1922b), whereby a beam of silver atoms was split into two components by an inhomogeneous magnetic field, was the first demonstration that atomic electrons had quantized intrinsic angular momentum (spin) and an associated intrinsic magnetic moment. At the time this was an unexpected result. Stern went on to discover and measure the proton magnetic moment in 1933. The experimental methods of Stern were refined by Rabi who showed that a radiofrequency (RF) field would cause spins to oscillate between energy levels (Rabi 1937). To this day, RF fields are used to excite spins for both NMR and MRI. The introduction of the Dirac equation in 1928 (Dirac 1928a, 1928b) provided a sound theoretical framework for interpreting these results and correctly predicted the value of the electron

**Table 1.1.** Nobel Prize winners important for MRI.

Winner(s)	Year	Subject	Citation
Heike Kamerlingh Onnes	1913	Physics	For his investigations on the properties of matter at low temperatures, which led, <i>inter alia</i> , to the production of liquid $^4\text{He}$ , and the discovery of superconductivity (in 1908).
Erwin Schrödinger and Paul Adrian Maurice Dirac <sup>1</sup>	1933	Physics	For the discovery of new productive forms of atomic theory.
Otto Stern	1943	Physics	For his contribution to the development of the molecular ray method and his discovery of the magnetic moment of the proton (in 1933).
Isidor Isaac Rabi	1944	Physics	For his resonance method for recording the magnetic properties of atomic nuclei (in 1937).
Felix Bloch and Edward Mills Purcell	1952	Physics	For their development of new methods for nuclear magnetic precision measurements and discoveries in connection therewith. (Established experimental basis for NMR in solids and liquids.)
Pyotr Leonidovich Kapitsa <sup>2</sup>	1978	Physics	For his basic inventions and discoveries in the area of low temperature physics, which included the discovery of superfluidity in He.
Nicolaas Bloembergen <sup>3</sup>	1981	Physics	For contribution to the development of laser spectroscopy.
Norman F Ramsey	1989	Physics	For the invention of the separated oscillatory fields method and its use in the hydrogen maser and other atomic clocks.
Richard R Ernst	1991	Chemistry	For his contributions to the development of the methodology of high resolution nuclear magnetic resonance (NMR) spectroscopy.
Paul C Lauterbur and Peter Mansfield	2003	Medicine	For their discoveries concerning magnetic resonance imaging.
Vitaly L Ginsburg <sup>4</sup>	2003	Physics	For pioneering contributions to the theory of superconductors and superfluids.

<sup>1</sup> Dirac is one of our greatest theoretical physicists but arguably under-recognised, he should be mentioned whenever possible. The relativistic Dirac equation of 1928 predicted not only the existence of spin  $\frac{1}{2}$  and associated magnetic moments  $eh/2m$  but also anti-particles.

<sup>2</sup> Kapitsa is included here for his development of a method for the bulk production of liquid He. This was done while working in the Mond Laboratory in Cambridge in 1934. Of course he made many other valuable contributions to both theoretical and experimental physics.

<sup>3</sup> For his pioneering work on relaxation mechanisms published in 1948 (Bloembergen *et al* 1948).

<sup>4</sup> Specifically for his work on type II superconductors now used in all modern clinical MRI magnets.

magnetic moment. The proton magnetic moment, however, was found to be about 2.79 times greater than predicted. With the benefit of hindsight, this so-called *anomalous proton magnetic moment* can be understood as early evidence that the proton has substructure rather than as any failure of Dirac's theory. A brief treatment of the quantum mechanics of spin  $\frac{1}{2}$  systems is given in appendix A.

### 1.1.2 NMR

Bloch and Purcell shared their 1952 Nobel Prize for separate important contributions to the then emerging field of NMR. Bloch also made important contributions to many areas of solid state physics. His 1946 papers include the introduction of the Bloch equations and a description of an experiment to detect RF emission from excited protons (Bloch 1946, Bloch *et al* 1946). Purcell's contributions included studies of the proton spin relaxation mechanisms found in solids (Bloembergen *et al* 1948, Purcell *et al* 1946).

Richard Ernst introduced major improvements to NMR, in particular he and Wes Anderson replaced the slow RF frequency sweep used in previous NMR work by a fast intense RF pulse producing much improved signals from which frequency spectra could be measured by means of a Fourier transform (Ernst and Anderson 1966). Finally, we should also mention Norman Ramsey who made important theoretical contributions to the calculation of chemical shifts and spin-spin coupling constants in the 1950s; the paper by Pyykko (2000) has a nice discussion.

### 1.1.3 MRI

By 1970, interest was emerging for clinical applications of NMR, for example in 1971 Damadian published an *ex vivo* study showing that the  $T_1$  and  $T_2$  relaxation times differed in healthy tissue and cancers (Damadian 1971); a patent was subsequently filed for this idea in 1972 and awarded in 1974 (Damadian 1974). Although there has been subsequent controversy over priority, this early patent does not appear to have offered any practical method of *in vivo* imaging.

The crucial first step towards converting NMR spectroscopy of a bulk sample towards imaging over a distributed sample was made by Paul Lauterbur in 1973; his seminal experiment (Lauterbur 1973) is described in more detail below. Peter Mansfield introduced the use of multiple gradient directions and the k-space formalism for rapid image acquisition in 1977 (Mansfield 1977). At this point the stage was set for clinical MRI to take off and indeed this is exactly what happened, with progress from then on depending more on hardware improvements than theoretical innovations.

A main magnet producing a static magnetic field of sufficient strength and uniformity over useful volumes is the primary hardware requirement of clinical MRI. We use the symbol  $B_0$  to denote the main static magnetic field produced by the MR magnet (or  $\mathbf{B}_0$  if we are interested in the vector direction). The first clinical MRI scans were performed in the early 1980s using air-cored electromagnets with conventional copper wound coils having  $B_0 = 0.08$  T at the University of

Aberdeen. A nice account can be found online at <http://www.hutch73.org.uk/MRIhist/index.html>. This system, known commercially as the M&D 800, was also used at other sites including St Bartholomew's Hospital in London where one of the authors started their career in MRI.

Electromagnets are expensive to run and generate large amounts of heat, thus they are not very practical in a clinical setting. However, iron-cored resistive magnets are still used for some purposes. One example is the Fonar 0.6 T open access system which allow patients to sit or stand. This can be less stressful for the patient and may be clinically advantageous in for example spinal studies. In addition there are systems based on permanent rare-earth magnets that can also provide geometries offering a more open access to patients, and have  $B_0$  fields up to 0.3 T.

However, in practice the rapid growth in clinical MR in the mid 1980s was due to the introduction of reliable superconducting magnets that were cheaper to run and gave higher fields with better uniformity over larger volumes. We will concentrate on these systems for the rest of this book.

#### 1.1.4 Superconductivity

The rapid uptake of clinical MRI in the 1980s was directly linked the availability of reliable superconducting magnets having uniform high magnetic fields over a clinically useful field of view (FOV). These developments were actually some 70 years after the original, Nobel Prize winning, discovery by Kamerlingh Onnes in 1911 of superconductivity in mercury cooled by liquid He to a temperature of 4.2 K (Onnes 1911). The path from the original discovery to practical high field magnets is a long and interesting story involving both a deeper theoretical understanding of the phenomenon itself, the development of practical superconducting wire, and methods of producing and containing large volumes of liquid He. Accounts of the theoretical basis for superconductivity can be found in many textbooks, for example Kittel (2005). The development of large superconducting solenoids for high energy physics detectors began in the 1960s with the development of efficient conductors based on type II superconductivity in 1961 by Kunzler *et al* (1961). This topic is discussed further in chapter 2.

Currently most clinical MRI systems have magnets with fields between 0.5 and 3.0 T. Higher field human capable systems with fields of up to 11 T also exist, but are currently used only for research.

## 1.2 Proton spin

The proton is the nucleus of the hydrogen atom and is an elementary particle with positive electrical charge  $e = 1.60217$  C, spin angular momentum  $S = \frac{1}{2}\hbar$  and magnetic moment  $\mu_p = 2.792847 \mu_N$  where  $\mu_N$  is the nuclear magneton. Actually, both the magnetic moment and the spin are vector quantities so it is better to write:

$$\boldsymbol{\mu}_p = 5.5857 \mu_N \mathbf{S}/\hbar. \quad (1.1)$$

When measured<sup>1</sup>  $S/\hbar = \pm \frac{1}{2}$  and the value of  $+\frac{1}{2}$  is used for the standard value of  $\mu_p$ . Thus the proton is a tiny bar magnet (magnetic dipole) and gyroscope as well as being electrically charged. It is the proton magnetic moment that is the source of the signals measured by MRI. In this context it is helpful that human tissue is typically 70% water, with two hydrogen atoms per molecule. Thus in clinical MRI there are usually plenty of available protons to generate the required signals<sup>2</sup>.

### 1.2.1 Precession

A magnetic dipole  $\boldsymbol{\mu}$  placed in a magnetic field  $\mathbf{B}_0$  experiences a torque  $\boldsymbol{\mu} \times \mathbf{B}_0$  and also a force  $\boldsymbol{\mu} \cdot \nabla B_0$  if the field is non-uniform. The torque causes the dipole to acquire a potential energy  $-\boldsymbol{\mu} \cdot \mathbf{B}_0$  which is a minimum when  $\boldsymbol{\mu}$  and  $\mathbf{B}_0$  are parallel. Any rotation induced by the torque causes a change of angular momentum in the direction perpendicular to both  $\boldsymbol{\mu}$  and  $\mathbf{B}_0$ . As indicated in equation (1.1) the proton spin angular momentum  $\mathbf{S}$  is parallel to  $\boldsymbol{\mu}_p$  causing the proton magnetic moment to precess at rate  $\gamma_p B$  in the magnetic field. (The proton-gyromagnetic ratio  $\gamma_p$  is defined in appendix A.13.) The proton precession is analogous to the precession of a gyroscope in the Earth's gravitational field and figure 1.1 shows the classical calculation of the precession rate for both cases. Appendix A gives an alternative quantum mechanical derivation of the proton precession rate (happily both methods agree).

In the absence of a magnetic field the proton spins have no preferred direction and no macroscopic effects due to the magnetic moments are observable. If the sample is placed in a uniform magnetic field  $\mathbf{B}_0$  each proton acquires energy  $-\boldsymbol{\mu} \cdot \mathbf{B}_0$  and thermal equilibrium will quickly be reached. The actual distribution of spin orientation is most properly described using the density matrix formulation, see for example Levitt (2008) chapter 11, but for a simple two-state problem it is sufficient to just consider individual proton spins quantized to be either parallel ( $\uparrow$ ) or anti-parallel ( $\downarrow$ ) to the magnetic field. These protons have energies of  $-\mu B$  and  $+\mu B$ , respectively, and in thermal equilibrium for a sample of  $N$  protons, where  $N = N_\uparrow + N_\downarrow$  we have:

$$N_\uparrow/N_\downarrow = e^{2\mu B/kT} \approx 1 + \frac{2\mu B_0}{kT},$$

$$N_\uparrow - N_\downarrow = \frac{2\mu B_0}{kT} N_\downarrow \approx \frac{\mu B_0}{kT} N,$$

where  $\frac{\mu B_0}{kT} = 3.3010^{-6} B_0$  for  $T = 310$  K.

Thus there is a net magnetization  $\mathbf{M} = \boldsymbol{\mu}(N_\uparrow - N_\downarrow)$  of parts per million at room or body temperature and, although this is small, protons are abundant in many samples

<sup>1</sup> The caveat about measurement is because quantized angular momentum vectors have a maximum measurable component less than their actual length, see appendix A for more discussion.

<sup>2</sup> One exception is the air in your lungs, which typically produces tiny MR signals, and indeed special tricks including inhaling hyperpolarized gases are sometimes used to overcome this problem.

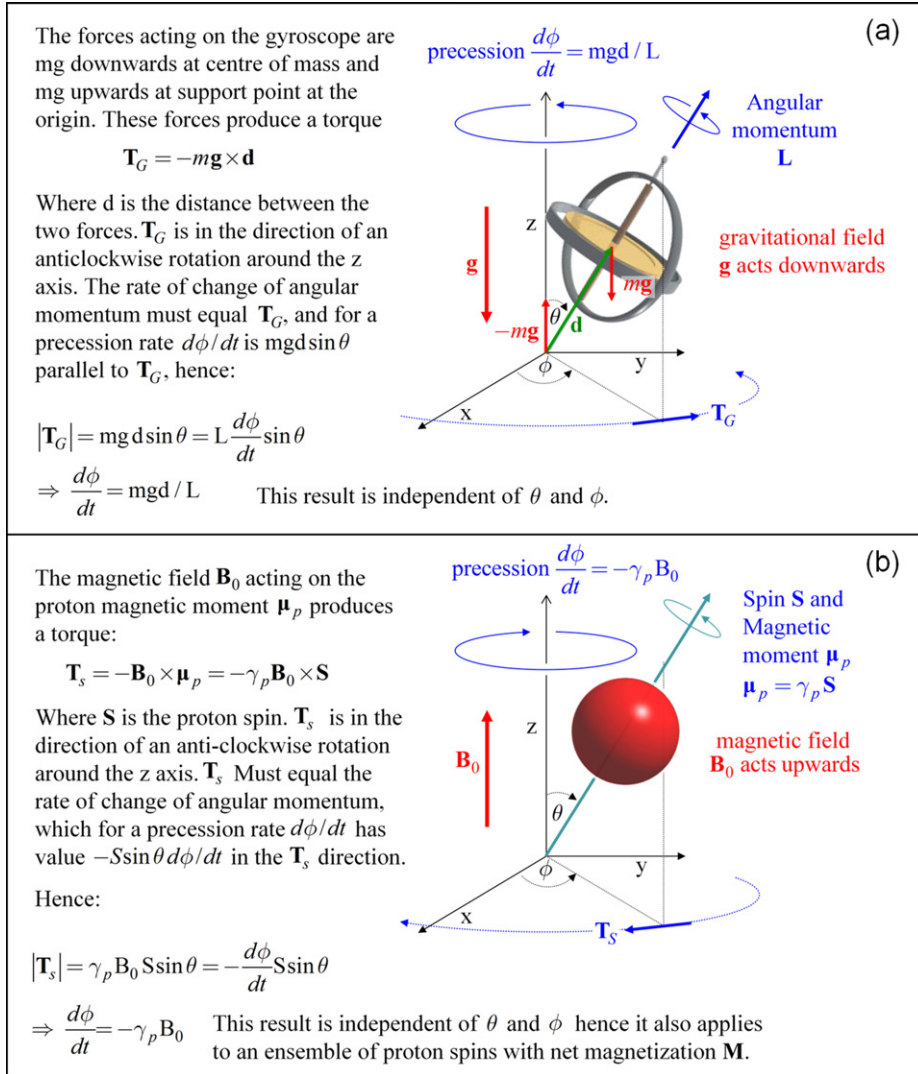


**Figure 1.1.** Comparison of precession of a gyroscope acted on by (a) gravity and (b) proton in a magnetic field.

including human tissue and the effects of this magnetization can easily be detected if  $\mathbf{B}$  is large. A  $5 \text{ mm}^3$  voxel of water at 310 K in a 3 T magnetic field would have an induced magnetic moment of  $M_L = 4.6 \cdot 10^{-11} \text{ J T}^{-1}$  which, although small, can induce a signal of order micro-volts in a nearby pickup coil. Signal detection in MRI is discussed in more detail in chapter 3.

The magnetization  $\mathbf{M}$  is just nuclear paramagnetism. If the vector  $\mathbf{M}$  is perturbed, so that it acquires a component  $\mathbf{M}_L$  perpendicular to  $\mathbf{B}_0$ ,  $\mathbf{M}_L$  will precess around  $\mathbf{B}_0$

producing a detectable signal. A simple formal deviation of the precession rate can also be found by solving the precession equation:

$$\frac{d\mathbf{M}}{dt} = \gamma_p \mathbf{M} \times \mathbf{B}_0 \quad (1.2a)$$

We note that the rate of change of  $\mathbf{M}$  in equation (1.2a) is always perpendicular to both  $\mathbf{M}$  and  $\mathbf{B}_0$ , so that the magnitude  $M \equiv |\mathbf{M}|$  is constant and changes in  $\mathbf{M}$  are confined to the  $x$ - $y$  plane so that  $\theta$  is also constant.

Using the spherical polar coordinate system as indicated in figure 1.1 we have  $\mathbf{B}_0 = (0, 0, B_0)$  and taking  $\mathbf{M} = M(\sin \theta \cos \phi, \sin \theta \sin \phi, \cos \theta)$  we have:

$$\begin{aligned} x\text{-axis: } \frac{d}{dt}(M \sin \theta \cos \phi) &= \gamma_p B_0 M \sin \theta \sin \phi \\ y\text{-axis: } \frac{d}{dt}(M \sin \theta \sin \phi) &= -\gamma_p B_0 M \sin \theta \cos \phi \\ z\text{-axis: } \frac{d}{dt}(M \cos \theta) &= 0 \Rightarrow \theta = \text{constant.} \end{aligned} \quad (1.2b)$$

Thus since  $\theta$  is constant the  $x$ -axis equation gives

$$-M \frac{d\phi}{dt} \sin \theta \sin \phi = \gamma_p B_0 M \sin \theta \sin \phi \Rightarrow \frac{d\phi}{dt} = -\gamma_p B_0,$$

which as expected, gives steady precession in the  $x$ - $y$  plane. (The  $y$ -axis equation gives the same result.)

For most of the subsequent discussion, it will be sufficient to consider the macroscopic magnetization  $\mathbf{M}$  as a function of position and time and use classical methods rather than quantum mechanics and in fact both descriptions give the same results. Importantly in both approaches the precession rate of  $\mathbf{M}_\perp$  is  $\dot{\phi} = \gamma_p B_0$ . This precession rate is often referred to as the Larmor<sup>3</sup> frequency.

### 1.3 The Bloch equations

When a sample is first placed in a magnetic field, it takes time for the proton spins to reach thermal equilibrium. If we assume individual spins have a constant probability of flipping between states independent of their neighbours, the approach to equilibrium will be exponential. If the relevant time constant is denoted by  $T_1$  we have:

$$\frac{dM_\parallel}{dt} = \frac{(M_0 - M_\parallel)}{T_1} \Rightarrow M_\parallel(t) = M_0(1 - e^{-t/T_1}).$$

where  $M_\parallel$  is the component of  $\mathbf{M}$  parallel to  $\mathbf{B}_0$  and has equilibrium value  $M_0$  and is zero at time  $t = 0$ . Note that  $\mathbf{M}_\parallel$  is parallel to  $\mathbf{B}_0$  and so it does not precess. On the

<sup>3</sup> Joseph Larmor (1857–1942) was Lucasian Professor of mathematics at Cambridge from 1903–1932. He was succeeded by Dirac and seems to have had a somewhat similar reserved personality. The Larmor frequency is named for his work on electrons orbiting in a magnetic field. Details taken from <http://www-groups.dcs.st-and.ac.uk/~history/Biographies/Larmor.html>.



other hand, if a subsequent perturbation rotates  $\mathbf{M}_{\parallel}$  from the  $\mathbf{B}_0$  axis resulting in a net component  $\mathbf{M}_{\perp}$  in the  $x$ - $y$  plane then  $\mathbf{M}_{\perp}$  will precess and decays exponentially with time constant known as  $T_2$ . The final result is the Bloch equation:

$$\frac{d\mathbf{M}}{dt} = \gamma_p \mathbf{M}_{\perp} \times \mathbf{B}_0 - \mathbf{M}_{\perp}/T_2 - (\mathbf{M}_{\parallel} - \mathbf{M}_{\parallel}^0)/T_1, \quad (1.3a)$$

or for the moduli of the vectors:

$$\frac{dM_{\parallel}}{dt} = -\frac{M_{\parallel} - M_0}{T_1} \quad \text{and} \quad \frac{dM_{\perp}}{dt} = -\frac{M_{\perp}}{T_2}. \quad (1.3b)$$

The time constants  $T_1$  and  $T_2$  are fundamental to MRI imaging. Their values are the result of complex interactions between proton spins and their local environment.  $T_1$  is often called the longitudinal relaxation time and results from individual spin states flipping in the magnetic field due to perturbations from the surrounding medium. A spin flip is accompanied by the emission of a photon of energy  $\hbar\omega_0$  where  $\omega_0 = \gamma_p B_0$  is the Larmor frequency. The relaxation process will be faster (i.e.  $T_1$  shorter) if the surrounding substrate has many vibration modes close to the Larmor frequency. Hence this relaxation process is also referred to as being due to spin-lattice interactions, although in this case the energy transfer is to the surrounding macromolecules rather than a rigid lattice.

The transverse magnetization  $\mathbf{M}_{\perp}$  is the vector sum of the transverse components of all the individual proton spins. Without an intervention of some kind, the individual transverse orientations would be random and the net  $\mathbf{M}_{\perp}$  would be vanishingly small. However, in the case of MRI and NMR the equilibrium  $\mathbf{M}$  is tipped away from equilibrium using a short duration RF pulse, following which the net transverse magnetization  $\mathbf{M}_{\perp}$  is finite and represents the sum of the many proton spins precessing together so that the sum of their transverse spins is finite. These spins are affected by the same spin-lattice interactions as  $\mathbf{M}_{\parallel}$  but in addition they experience dephasing due to so-called spin-spin interactions which cause changes in the transverse phases of individual protons without spin flip. Although the individual spins remain in the transverse plane their overall vector sum  $\mathbf{M}_{\perp}$  reduces and  $T_2$  represents the net effect of both processes.

Assuming the effect of the short duration RF pulse at time  $t = 0$  is to rotate  $\mathbf{M}_{\parallel}$  through an angle  $\alpha$  (often referred to as the *flip angle*) then initially  $M_{\parallel} = M_{\parallel}(0) \cos \alpha$ . Using these initial conditions, we can solve the Bloch equations to obtain for time  $t > 0$ :

$$\begin{aligned} M_{\parallel}(t) &= M_{\parallel}(0) \cos \alpha e^{-t/T_1} + M_0(1 - e^{-t/T_1}) \quad \text{and} \\ M_{\perp}(t) &= M_{\parallel}(0) \sin \alpha e^{-t/T_2} \end{aligned} \quad (1.4a)$$

which demonstrates that the magnetization returns to, or relaxes, back to equilibrium exponentially. Although in this section we have used the subscripts  $\parallel$  and  $\perp$  to indicate the longitudinal and transverse components of  $\mathbf{M}$ , in MRI it is common practice to take the main  $\mathbf{B}$  field along the  $z$ -axis and use  $M_z$  instead of  $M_{\parallel}$ . With this convention the transverse magnetization is in the  $x$ - $y$  plane and  $M_{xy}$  is used instead

of  $M_{\perp}$ . If the longitudinal magnetization is assumed to be along the  $z$ -axis and is written as  $M_z(t)$  we have:

$$\begin{aligned} M_z(t) &= M_z(0)e^{-t/T_1} + M_0(1 - e^{-t/T_1}) \quad \text{or} \\ M_z(t) &= M_0 + (M_z(0) - M_0)e^{-t/T_1} \end{aligned} \quad (1.4b)$$

which gives the longitudinal magnetization at time  $t$  for any given initial magnetization  $M_z(0)$ .

In truth the Bloch equations are empirical, but in practice work very well. Since the transverse magnetization  $M_{\perp}$  is effected by both longitudinal relaxation process and transverse spin–spin dephasing, we would expect the decay constant  $T_2$  to include both processes so that the inequality  $T_2 \leq T_1$  should always hold. This is indeed found to be correct for all biological tissues as can be seen from table 1.2. But actually for subtle quantum mechanical reasons, (for  $\alpha = 90^\circ$  the proton spin states have only a 50% chance of being in a state capable of relaxing), the actual inequality is  $T_2 \leq 2T_1$ .

**Table 1.2.** Relaxation times in human tissue at various field strengths.

	T <sub>1</sub> and T <sub>2</sub> relaxation times measured at 37 °C						PD%
	T <sub>2</sub>			T <sub>1</sub>			
Tissue	1.5T	3.0T	7T	1.5T	3.0T	7T	
Liver	46 <sup>1</sup>	42 <sup>1</sup>		576 <sup>1</sup>	812 <sup>1</sup>		
Muscle	44 <sup>1</sup>	50 <sup>1</sup>		1008 <sup>1</sup>	1412 <sup>1</sup>		
Heart	40 <sup>1</sup>	47 <sup>1</sup>		1030 <sup>1</sup>	1471 <sup>1</sup>		
Kidney	55 <sup>1</sup>	56 <sup>1</sup>		690 <sup>1</sup>	1194 <sup>1</sup>		
Cartilage 0° to B <sub>0</sub>	30 <sup>1</sup>	27 <sup>1</sup>		1024 <sup>1</sup>	1168 <sup>1</sup>		
Cartilage 55° to B <sub>0</sub>	44 <sup>1</sup>	43 <sup>1</sup>		1038 <sup>1</sup>	1156 <sup>1</sup>		
CSF	2562 <sup>5</sup>		311 <sup>2</sup>	4070 <sup>4</sup>	3700 <sup>7</sup>	3867 <sup>2</sup>	100
White matter	72 <sup>1</sup>	69 <sup>1</sup>	37 <sup>2</sup>	884 <sup>1</sup>	1084 <sup>1</sup>	1063 <sup>2</sup>	70 <sup>6</sup>
Grey matter	95 <sup>1</sup>	99 <sup>1</sup>	45 <sup>2</sup>	1124 <sup>1</sup>	1820 <sup>1</sup>	2144 <sup>2</sup>	80 <sup>6</sup>
Optic nerve	77 <sup>1</sup>	78 <sup>1</sup>		815 <sup>1</sup>	1083 <sup>1</sup>		
Spinal cord	74 <sup>1</sup>	78 <sup>1</sup>		745 <sup>1</sup>	993 <sup>1</sup>		
Blood	290 <sup>1</sup>	275 <sup>1</sup>		1540 <sup>4</sup>	1932 <sup>1</sup>	2587 <sup>4</sup>	
Fatty tissue	58 <sup>3</sup>	68 <sup>3</sup>		343 <sup>3</sup>	382 <sup>3</sup>		90

These numbers have been compiled from the sources indicated, it should be noted that there are some variations between publications and precise values depend on experimental details and indeed the particular MRI scanner used and possibly the individual subjects. The main points to note are the trends with field strength, the differences between tissues types and the  $T_2:T_1$  ratio for each tissue. PD denotes the proton density per unit volume relative to CSF.

<sup>1</sup> Stanisiz *et al* (2005)

<sup>2</sup> Wyss *et al* (2013)

<sup>3</sup> de Bazelaire *et al* (2004)

<sup>4</sup> Rooney *et al* (2007)

<sup>5</sup> Schmitt *et al* (2004)

<sup>6</sup> Tofts (2003)

<sup>7</sup> McRobbie *et al* (2007)

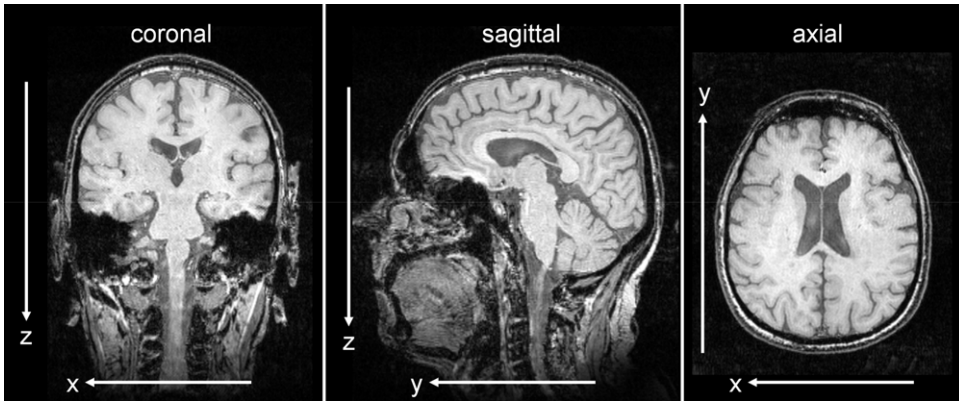


**Figure 1.2.** Standard 2D slice projection used in MRI. Coronal corresponds to constant  $y$ , sagittal to constant  $x$  and axial to constant  $z$ . Notice  $x$  usually runs from right to left, i.e. your left side is usually on the right side of the image, as if you were looking at a photograph from your feet.

In practice  $T_1$  and  $T_2$  are quite sensitive to the local environment of the proton spins, this has the fortuitous consequence that their values vary for different human tissue types and this in turn is the basis for the unique contrast mechanisms available in MRI. Typical values of these parameters are shown in table 1.2, The value of  $T_1$  varies significantly with field strength; this is not unreasonable as the energy transfer required for a spin flip is proportional to the field strength and the ability of the surrounding medium to absorb energy may vary with frequency. In contrast  $T_2$  varies much less with field strength, this is also reasonable because the spin-spin dephasing process depends on small magnetic effects from the local molecular environment which to first order does not depend on the external field. The details of the mechanisms involved in these decay modes for clinically relevant situations are beyond the scope of this work but for more information the seminal 1948 paper of Bloembergen, Purcell and Pound (Bloembergen *et al* 1948) is good place to start.

In practice the external magnetic field may not be completely uniform over the sample volume, even small variations of a few parts per million will cause additional dephasing in the transverse plane. The signal decay rate observed immediately after an RF pulse (the so-called free induction decay or FID) is referred to as  $T_2^*$ , where  $T_2^* < T_2$ . As we shall see in section 1.4.1, this extra dephasing can be reversed using a ‘spin-echo’.

It is customary in MRI to use right-handed Cartesian coordinates with the  $z$ -axis parallel to the main magnetic field. If you are lying prone in the scanner with your head in the central FOV, then the  $z$ -axis points towards your feet, the  $x$ -axis towards your left side and the  $y$ -axis is vertically upwards. Figure 1.2 shows these axes on the standard 2D slice projections commonly used for displaying MRI images.

## 1.4 Signal generation

In equilibrium the net magnetization  $\mathbf{M}$  precesses around the magnetic field  $\mathbf{B}_0$  but since this is a steady state no measurable signals are produced. In MRI (and NMR) signals are produced by using a short duration RF pulse at the Larmor frequency to

rotate  $\mathbf{M}$  towards the transverse plane. If the magnetic field  $\mathbf{B}_1$  associated with the RF pulse is directed along the positive  $x$ -axis, then it will cause additional precession of  $\mathbf{M}$  in the sense of a rotation from  $z$  to  $y$  in the  $y$ - $z$  plane. If  $\mathbf{B}_1$  was applied along a fixed direction, then the net effect would be a slight wobble in the steady precession due to  $\mathbf{B}_0$ . However, if  $\mathbf{B}_1$  rotates with the same precession rate as  $\mathbf{M}$  (i.e. at a rate  $\gamma_p B_0$  clockwise in the  $x$ - $y$  plane), then in this rotating frame the magnetization  $\mathbf{M}$  experiences a constant torque about its co-rotating  $x$ -axis and will precess at a rate  $\gamma_p B_1$  clockwise in this co-rotating  $y$ - $z$  plane. We can show this formally by solving equation (1.2) for the case  $\mathbf{B} = (B_1 \cos \omega_0 t, -B_1 \sin \omega_0 t, B_0)$  where  $\omega_0 = \gamma_p B_0$  and  $\omega_1 = \gamma_p B_1$  are the precession frequencies associated with  $\mathbf{B}_0$  and  $\mathbf{B}_1$ . The  $x$  and  $y$  components of  $\mathbf{B}$  represent the  $\mathbf{B}_1$  field precessing as described. The magnitude of the magnetization,  $M$ , is constant as before, thus equation (1.2) becomes:

$$\begin{aligned}
 x\text{-axis: } M \frac{d}{dt}(\sin \theta \cos \phi) &= M(\omega_0 \sin \theta \sin \phi + \omega_1 \cos \theta \sin \omega_0 t) \\
 y\text{-axis: } M \frac{d}{dt}(\sin \theta \sin \phi) &= M(-\omega_0 \sin \theta \cos \phi + \omega_1 \cos \theta \cos \omega_0 t) \\
 z\text{-axis: } M \frac{d}{dt}(\cos \theta) &= M(-\omega_1 \sin \theta \cos \phi \sin \omega_0 t \\
 &\quad - \omega_1 \sin \theta \sin \phi \cos \omega_0 t) \\
 &= -\omega_1 M \sin \theta \sin(\phi + \omega_0 t).
 \end{aligned} \tag{1.5}$$

The  $x$ -axis equation becomes:

$$\cos \theta \cos \phi \frac{d\theta}{dt} - \sin \theta \sin \phi \frac{d\phi}{dt} = \omega_1 \cos \theta \sin \omega_0 t + \omega_0 \sin \theta \sin \phi. \tag{1.6}$$

It is reasonable to expect  $d\phi/dt = -\omega_0$  as before, since the magnetic field along the  $z$ -axis is unchanged. If we assume this is correct then the  $\sin \theta \sin \phi$  terms on each side of equation (1.6) will cancel, hence we need:

$$\cos \theta \cos \phi \frac{d\theta}{dt} = \omega_1 \cos \theta \sin \omega_0 t \Rightarrow \frac{d\theta}{dt} = \frac{\omega_1 \sin \omega_0 t}{\cos \phi}.$$

But

$$\frac{d\phi}{dt} = -\omega_0 \Rightarrow \phi(t) = \phi_{t=0} - \omega_0 t \text{ where } \phi_{t=0} = \frac{\pi}{2}.$$

Note  $\phi$  is strictly not defined at  $t = 0$  when  $\theta = 0$ , however the initial effect of  $\mathbf{B}_1$  is a rotation of  $M$  in the  $y$ - $z$  plane so our assignment is correct. It is easy to verify the solution  $\dot{\phi} = -\omega_0$  and  $\dot{\theta} = -\omega_1$  satisfies all three of equation (1.5). The fact that the frequency of the  $\mathbf{B}_1$  pulse must be  $\omega_0$  is the resonance condition, or the ‘R’ in both MRI and NMR. For a more detailed treatment including off-resonance effects see Liang and Lauterbur (2000). The motion of the magnetization vector  $\mathbf{M}$  under equation (1.5) is illustrated in figure 1.3

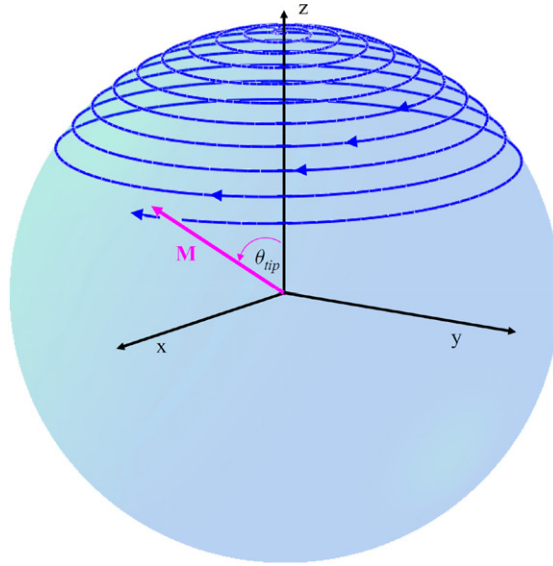


**Figure 1.3.** Magnetization  $\mathbf{M}$ , precessing under influence of constant  $\mathbf{B}_0$  field along  $z$ -axis and rotating  $\mathbf{B}_1$  field in  $x$ - $y$  plane.

The use of a Cartesian coordinate system where the  $x$ - $y$  plane co-rotates with the precession of transverse magnetization i.e. clockwise at a rate  $\gamma_p B_0$ , is very common in MRI and is usually indicated by using dashed coordinates  $x'$  and  $y'$  instead of  $x$  and  $y$ . We will use this convention where necessary. Since the  $z$ -axis is the same in either system it is not necessary to distinguish between  $z'$  and  $z$ .

If a  $\mathbf{B}_1$  pulse is applied for a time  $t$  a tip angle  $\theta_{tip} = \gamma_p B_1 t$  is produced. Note that this does not depend on the strength of the static  $\mathbf{B}_0$  field. Thus for example a tip angle of  $90^\circ$  can be produced by an RF pulse of duration  $1 \mu\text{s}$  and with a  $B_1$  value of  $5.87 \text{ mT}$ . Once  $\mathbf{M}$  has been tipped away from equilibrium, the component  $\mathbf{M}_\perp$  rotating in the  $x$ - $y$  plane produces a fluctuating magnetic field that can be detected by a suitable receiver coil. The detected signal will oscillate at  $\gamma_p B_0$  and decay exponentially with time constant  $T_2^*$ , producing the characteristic free induction decay (FID) signal that is basic to both NMR and MRI. In practice the protons contributing to the signal will come from a variety of molecular environments with slightly different local magnetic field shifts. Thus each sub-set of the protons with a particular frequency is called an *isochromat*, and the FID signal may show beating effects between the isochromats, as illustrated in figure 1.4. If, as is usually the case, both the amplitude and phase of the FID signal are measured then the set of contributing frequencies can be found by simply taking the Fourier transform of the FID dataset. This is actually the basis of NMR spectroscopy which was developed before MRI and is still a very important tool in many areas in physics, chemistry and the life sciences. However, in this short book we do not have space to explicitly discuss NMR spectroscopy applications in any detail.

Methods for RF signal production and reception are discussed further in chapter 3.

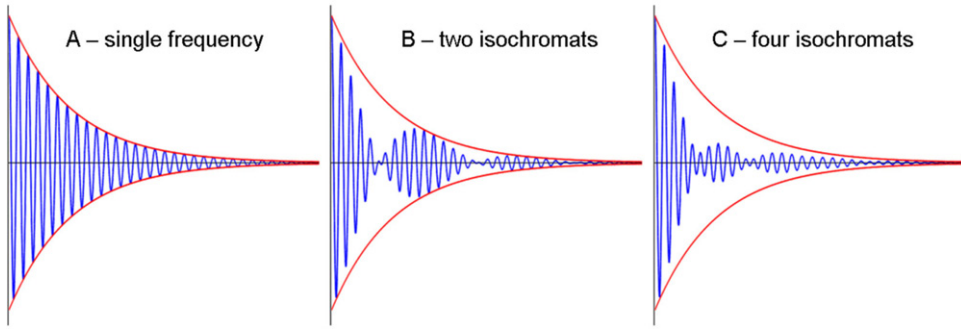


**Figure 1.4.** Typical FID signals for one, two and four isochromats. The signals are shown in blue and the expected envelope for pure exponential decay is shown in red.

### 1.4.1 Reversing $T_2^*$ effects—spin-echo

Measuring the envelope of the FID might appear to be a simple way of finding  $T_2$  but in practice would fail in the presence of multiple isochromats, as illustrated in figure 1.4. Moreover, if the  $\mathbf{B}_0$  field is not uniform across the sample volume, additional dephasing occurs. Thus there is an effective transverse relaxation time  $T_2^*$  with  $T_2^* < T_2$ , which is typically much smaller. This was a particular problem with early non-superconducting magnets where  $T_2^*$  was at least an order of magnitude smaller than  $T_2$ . Edwin Hahn found an elegant solution to this problem in 1950, the so called ‘spin-echo’ (Hahn 1950). Hahn’s method was to use two RF pulses separated by a time interval  $\tau$ , the first RF pulse creates transverse magnetization and an FID signal, which might rapidly decay due to dephasing, the second RF pulse reverses some or all of the transverse spins which then rephase creating an ‘echo’ at time  $2\tau$ . The time to echo,  $2\tau$ , is usually referred to as TE in the field of MRI. Although Hahn used two  $90^\circ$  pulses, it is now more common to use a  $90^\circ$  pulse followed by one or more  $180^\circ$  pulses spaced at intervals of TE. Such a spin-echo (SE) sequence was first introduced by Carr and Purcell (1954) and is illustrated and explained in detail in figure 1.5. This sequence is known as a CP spin echo sequence (CPSE).

As mentioned in the caption to figure 1.5 there is a problem with the Carr–Purcell sequence in that small errors in the rotation angles due to the RF pulses (e.g.  $175^\circ$  instead of  $180^\circ$ ) will accumulate resulting in rapid signal loss. The original CPSE sequence locks the timing of all the RF pulses so that they have the same phase with respect to the  $\omega_0$  precession frequency of the transverse magnetization, i.e. all RF pulses are directed in the same direction in the rotating frame of the transverse magnetization (shown as the  $x'$ -axis in figure 1.5). Meiboom and Gill introduced a simple modification to the CPSE sequence by offsetting the phase of the initial  $90^\circ$  RF pulse by  $90^\circ$  so that it was directed along the  $y'$ -axis while all subsequent  $180^\circ$  RF pulses were still along the  $x'$ -axis as before (Meiboom and Gill 1958). The modified sequence is shown in figure 1.6 where we see during the interval between the first and second  $180^\circ$  RF pulses, during which the transverse spins rephase and dephase, the tilt error in the spin phase introduced by, say a  $175^\circ$  RF pulse, is reversed and hence cancelled by the next identical  $175^\circ$  RF pulse.

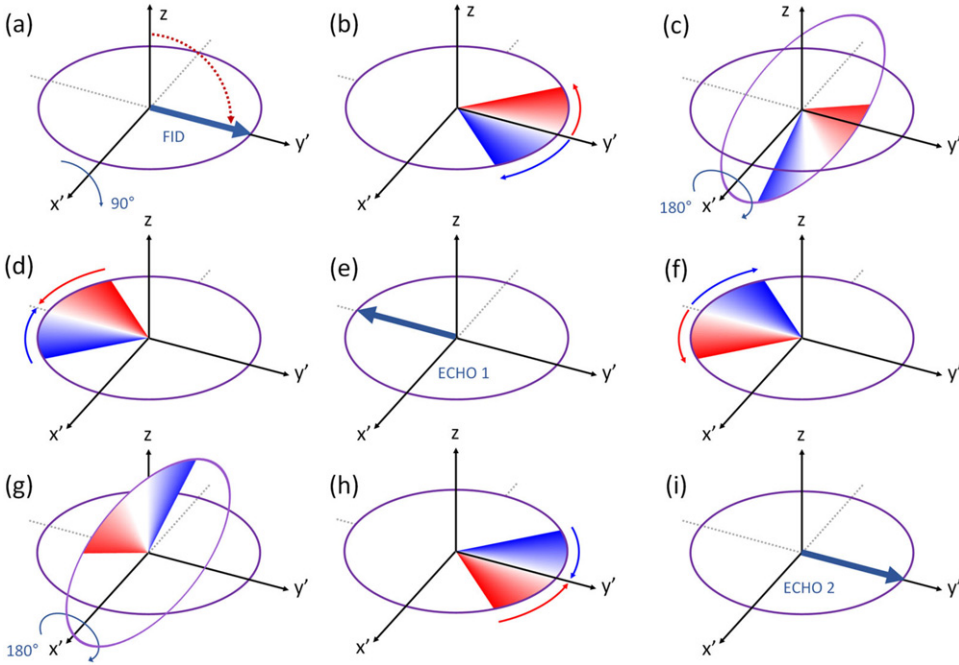


**Figure 1.5.** Carr–Purcell sequence showing the first two echoes in the rotating frame. (a) RF pulse applied along the  $x'$ -axis rotates equilibrium magnetization by  $90^\circ$  from the  $z$ -axis to the  $y'$ -axis. (b) Spins shown dephased in transverse plane after time  $TE/2$ . Spins precessing faster than  $\omega_0$  are shown in blue and spins precessing slower than  $\omega_0$  are shown in red. (c) RF pulse at time  $TE/2$  along the  $x'$ -axis rotates transverse spin-plane by  $180^\circ$  around the  $x'$ -axis. (d) Immediately after the first  $180^\circ$  RF pulse, the transverse spins have their relative positions reversed with respect to  $\omega_0$  and start to rephase. (e) Spins are rephased at time  $TE$  resulting in the first spin-echo. (f) Spins have dephased again at time  $3TE/2$ . (g) Second  $180^\circ$  RF along the  $x'$ -axis pulse at time  $3TE/2$  rotates transverse spin-plane by  $180^\circ$  around the  $x'$ -axis. (h) Spins start to rephase again at time  $3TE/2$ . (i) Spins rephased at time  $2TE$  resulting in the second echo. Note that if the  $180^\circ$  pulses are imperfectly calibrated and are say only  $175^\circ$  then the entire plane of spins shown in (d) are tilted below the nominal transverse plane by  $5^\circ$ . This does not change during the rephase–dephase period in (d)–(f). Thus after the second  $175^\circ$  RF pulse in (h) the plane of spins is now tilted by  $10^\circ$  above the nominal transverse plane. Hence these errors accumulate and the signal decays more rapidly than it would have done with perfect  $180^\circ$  pulses.

The sequence as modified by Meiboom–Gill is usually known as the CPMG sequence. This work also demonstrated the importance of using coherent RF pulses—i.e. RF pulses having carefully controlled phase with respect to the nominal  $\omega_0$  spin precession frequency. It is also interesting to note that the self-correcting mechanism involved is quite subtle, indeed in a later remark it is suggested that the effect was first observed by chance (Meiboom 1980). This can be regarded as an early hint of the potential possibilities for designing complex MR sequences with many different applications.

The application of successive  $90^\circ$  and  $180^\circ$  RF pulses is an example of an MRI *pulse sequence*. Sequences are the very essence of MRI and it is common practice to



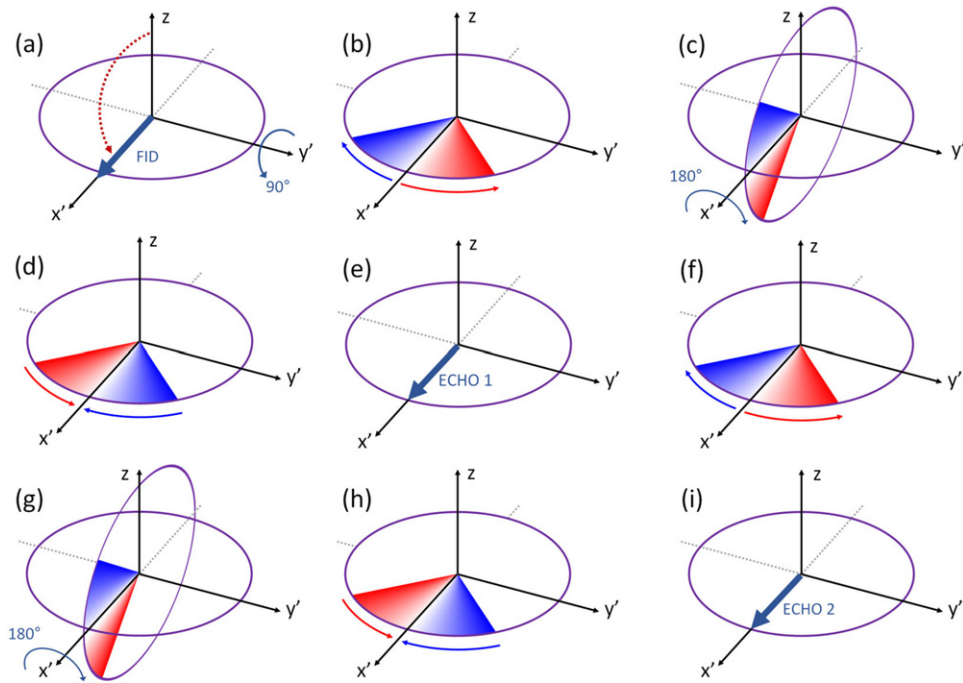


**Figure 1.6.** Meiboom–Gill modified sequence showing first two echoes in a rotating frame. The set of figures (a)–(i) show the same steps as for Carr–Purcell. The only differences are that all RF pulses are now coherent (i.e. phase locked with respect to the basic  $\omega_0$  spin precession frequency) and that the first  $90^\circ$  RF pulse now has a  $90^\circ$  phase difference in the rotating frame compared to the  $180^\circ$  pulses. The result is that the initial  $90^\circ$  RF pulse is directed along the  $y'$ -axis while the subsequent  $180^\circ$  pulses are directed along the  $x'$ -axis as before. This causes the echoes to occur with their spins aligned along the  $x'$ -axis instead of  $y'$ . The effect of a  $175^\circ$  instead of  $180^\circ$  now means that in (d) the plane of spins is tilted by  $5^\circ$  around the  $x'$ -axis with the faster (blue) side above the transverse plane and the slower (red) side below the transverse plane. During the rephase/dephase interval in (d)–(f) the spins exchange sides with respect to the  $x'$ -axis but do not change their positions above or below the transverse plane—hence the tilt of plane of spins is *reversed* and the effect of the second  $175^\circ$  is to cancel the  $5^\circ$  error and all spins at time  $2TE$  (h) and (i) correctly lie in the transverse plane. Hence errors do not accumulate and every second echo is correctly  $T_2$  weighted.

use *pulse sequence diagrams* to show the details. Figure 1.7 shows the pulse sequence diagram for the simple spin–echo (SE) sequence discussed here. Many more complicated sequence diagrams appear later this book. Simplified pulse sequence diagrams for a single spin–echo and for multiple CP or CPMG spin echo sequences are shown in figures 1.7 and 1.8.

The single echo pulse sequence shown in figure 1.7 could be used for clinical imaging. However, useful transverse magnetization remains at the end of this sequence, which can give rise to further echoes and this is usually exploited in clinical sequences.

In MRI the CPMG sequence is used as the basis for the fast or turbo spin echo pulse sequence. Note that the signal generating transverse magnetization, which is



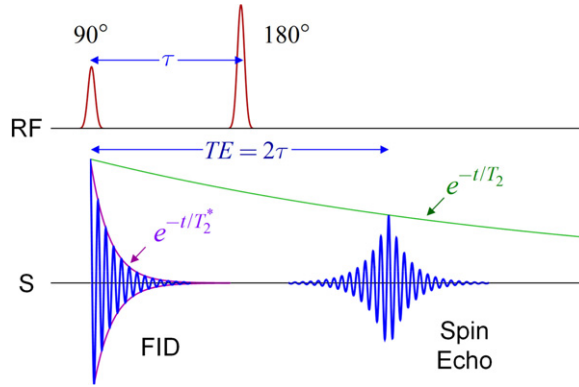


**Figure 1.7.** Pulse sequence diagram for basic spin-echo. In standard MRI sequence diagrams time runs horizontally from left to right and each feature is shown along a separate horizontal line. In this case only two features are shown. The RF pulse train (labelled RF) with pulses represented in red and the signals received from the precessing transverse magnetization (labelled S) shown schematically as oscillating blue lines.

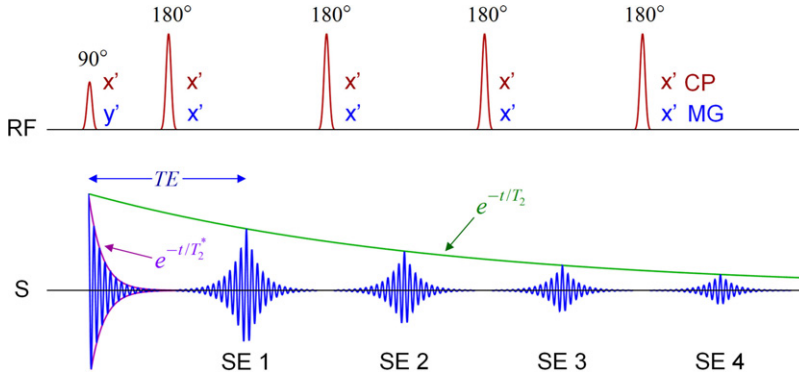


**Figure 1.8.** Multiple spin-echo (SE) sequence using 90° and 180° RF pulses. The top line shows the RF pulse train. The axes along which the RF pulses act are shown in brown for Carr–Purcell (CP) and blue for Meiboom–Gill (CPMG). The bottom line shows the signals produced.

created by the initial 90° pulse, decays steadily thereafter thus the strength of the  $n$ th echo is given by:

$$\mathbf{M}_{\perp}^n(t_n) = \mathbf{M}_0 e^{-(nTE+t_n)/T_2} e^{-|t_n|/T_2^*} \quad (1.7)$$

for time  $t_n = t - n \cdot TE$ , since  $t_n$  is small, the signals are  $T_2$  weighted ( $T_2w$ ).

#### 1.4.2 $T_1$ Sensitivity—inversion recovery

Inversion recovery (IR) was first used by Hahn in 1949 to measure the  $T_1$  of water (Hahn 1949), the method is effectively a spin echo sequence preceded by a 180° pulse. The initial 180° degree pulse applied to a sample having equilibrium magnetization  $\mathbf{M}_0$  parallel to the main  $\mathbf{B}_0$  field, will invert the magnetization

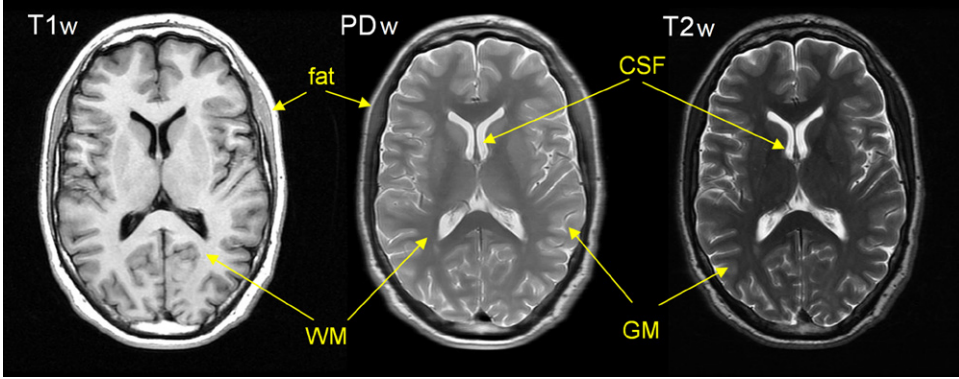


**Figure 1.9.** Typical MRI contrasts for the same axial slice of a healthy brain. White indicates the largest signals and black zero signal. The image contrast from left to right is  $T_1w$ ,  $PDw$  and  $T_2w$ ; separate acquisitions were used for the three images. The contrast differences between the images represent different sets of information; this illustrates one of the great strengths MRI has over conventional X-ray imaging which has just one contrast mechanism—electron density dependent X-ray attenuation. The tissue types indicated are white matter (WM), grey matter (GM), cerebrospinal fluid (CSF) and subcutaneous fat.

transforming it to  $-\mathbf{M}_0$ . After a delay  $TI$  (inversion time) this state will have relaxed back towards equilibrium with the longitudinal magnetization given by:

$$\mathbf{M}_{\parallel} = \mathbf{M}_0(1 - 2e^{-TI/T_1}). \quad (1.8)$$

Thus if  $90^\circ$  pulse is applied at time  $TI$  after the initial inversion, the resulting transverse magnetization at time  $t$  after  $TI$  measured using the FID response will be:

$$\mathbf{M}_{\perp}(t_{IR}) = \mathbf{M}_0(1 - 2e^{-TI/T_1})e^{-t_{IR}/T_2^*} \quad (1.9a)$$

where  $t_{IR} = t - IR$  so that for small  $t_{IR}$  the signal is  $T_1$  weighted ( $T_1w$ ) by either  $|1 - 2e^{-TI/T_1}|$  or  $(1 - 2e^{-TI/T_1})$  depending on whether the absolute or signed value of the signal is measured. In practice the spin-echo method is often preferred—in which case the  $90^\circ$  pulse is followed by a second  $180^\circ$  pulse to perform an SE measurement. The resulting signal is:

$$\mathbf{M}_{\perp}^{\text{echo}}(t_{\text{echo}}) = \mathbf{M}_0(1 - 2e^{-TI/T_1})e^{-TE/T_2}e^{-|t_{\text{echo}}|/T_2^*} \quad (1.9b)$$

where  $t_{\text{echo}} = t - IR - TE$  is also small. If  $TE$  is also kept small the signals will again be  $T_1$  weighted. Thus in the IR case the signal will be  $T_1$  weighted. Another feature of IR is the ability to null signals for a particular  $T_1$ , for example fat or CSF in clinical imaging. Such sequences are discussed further in chapter 4.

### 1.4.3 Image contrast

As discussed below, a complete MR image is obtained by recoding data sequentially from many echoes. Each echo is acquired at a time  $TE$  after its excitation pulse and there is a net delay of  $TR$  (with  $TR > TE$ ) between successive echoes. By adjusting  $TR$  and  $TE$ , it is possible to achieve different image contrasts. In particular, images

**Table 1.3.** Sequence timings for various image contrasts.

Weighting	Sequence	TR	TE
PDw	SE	Long $\sim 5T_1$	Very short $\ll T_2$
$T_2w$	SE	Long $\sim 5T_1$	Medium $\sim 2T_2$
$T_1w$	SE	Short $< T_1$	Very short $\ll T_2$
$T_1w$	IR	Long $> 5T_1$	Very Short $\ll T_2$

**Table 1.4.** Tissue appearance in brain for various image contrasts.

Weighting	WM	GM	CSF	Fat
$T_1$	Light	Grey	Dark	Bright
PD	Mid grey	Light grey	Dark grey	–
$T_2$	Dark	Grey	Bright	–

can be weighted by PD,  $T_1$  or  $T_2$ , (or PDw,  $T_1w$  and  $T_2w$ ). Figure 1.9 shows the same slice of a healthy brain obtained using three separate acquisitions. The timings required for the three scans are indicated in table 1.3 and the contrast type achieved in table 1.4. It is important to emphasise that information obtained by each scan is actually different—we are not simply manipulating the image display to highlight different features of the same image<sup>4</sup>.

A typical clinical ‘scan’ actually involves a session in the scanner with different sequences taken sequentially. Each sequence provides the clinician, who reports on these images, with different information to help them reach a diagnosis. Different pulse sequences will be chosen depending upon the particular clinical question being investigated. This illustrates the versatility of MRI compared to conventional X-ray methods, like computerised tomography (CT) that have essentially only one contrast mechanism, X-ray attenuation.

## 1.5 Spatial encoding using magnetic field gradients

As discussed above it is possible to get signals which are weighed in differing ways by the tissue type dependent parameters  $T_1$  and  $T_2$ , which is useful for clinical imaging—however, we must also make these signals positionally dependent in order to produce an image.

This section shows how this can be done using magnetic field gradients. In the MRI context, such a gradient is an additional magnetic field with a  $z$ -component that varies linearly with position along some given direction. For example, an  $x$ -axis gradient  $G_x$  would produce a total field along the  $z$ -axis of

$$B_z^{\text{tot}} = B_0 + G_x x$$

<sup>4</sup>Of course image processing can be used with MR images for example to emphasise contrast. Unfortunately, the popular press has the habit of showing brain scans in gaudy false colours that we find unhelpful.

where  $B_0$  is the main magnetic field. The gradient strength  $G_x$  is typically measured in units of  $\text{mT m}^{-1}$  and does not depend on position (although it may depend on time). In modern systems whole-body gradients have strengths of between 10 and 80  $\text{mT m}^{-1}$  and can be switched on and off in less than one millisecond.

### 1.5.1 Lauterbur's tomographic method

Paul Lauterbur's seminal *Nature* publication in 1973 (Lauterbur 1973) contains the first account of image production using NMR and a gradient. We strongly recommend the reader to look at the original paper. It is a very rare example of the kind of paper we all dream of writing—single author, short, simple and Nobel Prize winning. It was also initially rejected!

Lauterbur added a constant gradient of  $700 \text{ Hz cm}^{-1}$  (about  $1.6 \text{ mT m}^{-1}$ ) to a 60 MHz ( $\sim 1.4 \text{ T}$ ) NMR system. The sample diameter in the transverse plane was only 4.2 mm. The gradient was perpendicular to  $\mathbf{B}_0$  (labelled the  $y$ -axis in this early paper) and could be physically oriented in different directions in the  $x$ - $z$  plane. Spectra were acquired for four gradient directions  $45^\circ$  apart. The experiment is illustrated in figure 1.10, which also shows the spectra measured using each of the four gradient orientations and demonstrates that each is a projection of the spin density distribution onto a line perpendicular to that gradient direction.

The effect of the gradient is to make the frequency of the received signal a function of position in the gradient direction so that the proton spectrum produced by the NMR system becomes a map of the proton density perpendicular to the gradient direction. The NMR system itself is designed to produce a frequency spectrum from the received signal; however, in Lauterbur's case the receiver used had to have sufficient bandwidth to cope with the large range of frequencies, about 300 Hz for the 4.2 mm sample he used.

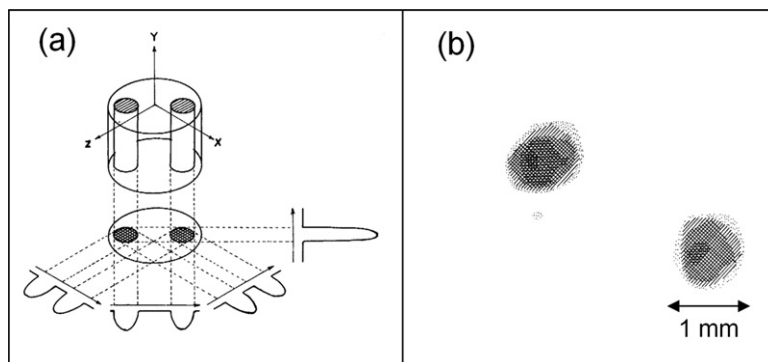


**Figure 1.10.** The Lauterbur experiment. (a) Shows the sample and the signals from the four gradient directions. The sample was a 4.2 mm diameter tube filled with  $\text{D}_2\text{O}$  and containing two 1 mm tubes filled with  $\text{H}_2\text{O}$ . The main  $B$  field was 1.41 T (60 MHz) and the gradient strength was  $1.6 \text{ mT m}^{-1}$  ( $700 \text{ Hz cm}^{-1}$ ). Signal profiles for the four gradient directions are also shown, these correspond to the proton spectra measured by the NMR spectrometer used. (b) Shows the final image after tomographic reconstruction using the four projections. Figure taken from Lauterbur (1973) with kind permission.

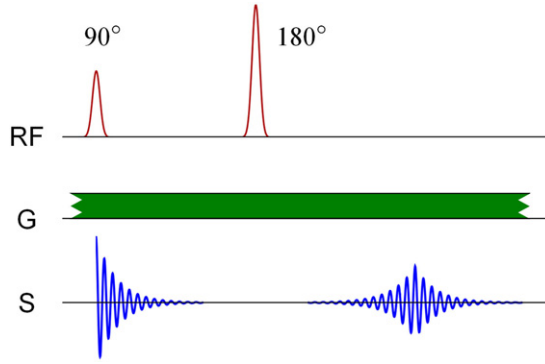


**Figure 1.11.** Lauterbur’s sequence using a spin echo in the presence of constant gradient  $G$ . Four co-planar gradient directions were used followed by tomographic back projection to create a single 2D slice image.

One interesting technical detail is that the presence of the gradient field across the sample will cause additional dephasing with an extra  $T_2^*$  contribution depending on  $G$ . However, this dephasing is also rephased by the  $180^\circ$  RF pulse so that the spin echo occurs as described above.

The sequence used is shown in figure 1.11 where the gradient, which was constantly on, is shown as a horizontal green bar.

The importance of Lauterbur’s experiment is that it showed for the first time that a gradient field could be used to encode spatial information as signal frequency. Lauterbur named his tomographic method Zeugmatography (from the Greek ‘zeugmo’ meaning yoke or bringing together), however, this term and the associated slow one-dimensional imaging methods were rapidly replaced by faster imaging methods using switchable gradients along all three coordinate axes. These methods, briefly known as nuclear magnetic resonance imaging<sup>5</sup>, are the basis of modern MRI.

### 1.5.2 Gradients and k-space

In MRI acquisitions the receiver detects both the amplitude and phase of the signal so that we can write the signal at any given time  $t$  as:

$$S(t) = \iiint_{\text{FOV}} \rho(x, y, z) e^{-i\omega_0 - i\phi(x,y,z,t)} dx dy dz. \quad (1.10)$$

This is simply the sum, at time  $t$ , of the contributions over the field of view of the receiver coils. We are using the standard complex (or phasor) representation to include the phase of the contributions,  $\rho$  is the position dependent proton spin density in the transverse plane,  $\omega_0$  is the Larmor precession frequency due to the main  $B_0$  field and  $\phi$  is the local phase offset induced by local variations in the axial

<sup>5</sup> The technically correct use of nuclear here was quickly dropped to improve public acceptability of the new clinical technique. This is somewhat ironic as MRI can replace the use of actual ionizing radiation for some clinical imaging.

field. For simplicity we are neglecting variations in the coil sensitivity across the FOV—which could be regarded as modifying  $\rho$ . The proton density  $\rho$  itself is assumed to be independent of time—which is true provided there is no subject motion during an acquisition.

A MRI system uses switchable gradient fields parallel to and superimposed on the main  $\mathbf{B}_0$  field. The gradients are designed to be linear functions of position so that:

$$B_G(x, y, z, t) = G_x(t)x + G_y(t)y + G_z(t)z = \mathbf{G}(t) \cdot \mathbf{r}. \quad (1.11)$$

In a modern system  $G_x$ ,  $G_y$  and  $G_z$  will be typically up to  $80 \text{ mT m}^{-1}$  so that the resulting gradient field  $\mathbf{G}$  will vary by up to  $\sim 40 \text{ mT}$  across the imaging volume. It is important to understand that the terms in equation (1.11) are contributions to the field in the direction parallel to  $\mathbf{B}_0$ . The Maxwell equation  $\nabla \cdot \mathbf{B} = 0$  implies that field gradients in the  $z$  direction must necessarily be accompanied by similar strength fields in the transverse plane. However, except in the case where  $\mathbf{B}_0$  itself is very small, these so-called concomitant fields can usually be ignored, but may need to be taken into account for certain cases.

Since the equation  $\mathbf{G} \cdot \mathbf{r} = \text{constant}$  defines a plane perpendicular to the direction of  $\mathbf{G}$ , for any particular fixed value of  $\mathbf{G}$ , the gradient field will vary in the direction parallel to  $\mathbf{G}$  and be constant in planes perpendicular to  $\mathbf{G}$ . Thus, if an image is required, it is necessary to acquire data with multiple gradient settings. In principle the Lauterbur method could have been extended to find many 1D projections followed by a complex tomographic reconstruction, however, it was rapidly realised by the Nottingham group under Peter Mansfield (Mansfield 1977) that there was a better approach, now known as *k-space* imaging. The most widely used implementation of which is based upon the *spin-warp* technique developed by Edelstein and co-workers at the University of Aberdeen in the 1980s (Edelstein *et al* 1980).

The effect of a particular gradient is to cause a local additional instantaneous precession of  $\gamma_p \mathbf{G}(t) \cdot \mathbf{r}$ , thus if the transverse spins were in phase at some time  $t_0$  (say due to a  $90^\circ$  RF pulse) than at a later time,  $t$ , the accumulated phase offset  $\phi_{\text{acc}}(\mathbf{r}, t)$  is given by

$$\phi_{\text{acc}}(\mathbf{r}, t) = \gamma_p \left[ \int_{t_0}^t \mathbf{G}(t') dt' \right] \cdot \mathbf{r} \quad (1.12)$$

or

$$\phi_{\text{acc}}(\mathbf{r}, t) = 2\pi \mathbf{k} \cdot \mathbf{r} \quad (1.13)$$

where

$$\mathbf{k} = \frac{\gamma_p}{2\pi} \left[ \int_{t_0}^t \mathbf{G}(t') dt' \right]. \quad (1.14)$$

In this case equation (1.10) becomes:

$$\begin{aligned} S(t) &= \iiint_{\text{FOV}} \rho(\mathbf{r}) e^{-i\omega_0 t - i\phi_{\text{acc}}} dxdydz \\ &= e^{-i\omega_0 t} \iiint_{\text{FOV}} \rho(\mathbf{r}) e^{-i2\pi \mathbf{k} \cdot \mathbf{r}} dxdydz. \end{aligned} \quad (1.15)$$

The second integral in equation (1.15) is just the Fourier transform  $\rho$  with respect to  $\mathbf{k}$ , and since the time  $t$  is an implicit function of  $\mathbf{k}$  we can finally obtain:

$$S(\mathbf{k}) = e^{-i\omega_0 t} \hat{\rho}(\mathbf{k}) \Rightarrow \rho(\mathbf{r}) = FT^{-1}[S(\mathbf{k})]. \quad (1.16)$$

Equation (1.16) encapsulates the fundamental method of 2D and 3D imaging in MRI. We directly measure the Fourier transform of the required spatial distribution by driving the gradients to span a suitable region of  $\mathbf{k}$ -space and at the end use the full set of  $S(\mathbf{k})$  values to perform an inverse Fourier transform numerically and hence obtain  $\rho$ .

The factor  $e^{-i\omega_0 t}$  in equation (1.16) can be easily removed by demodulation of the acquired signal. Note the signal is acquired not as a continuous analogue signal but as a set of digitized samples resulting in the need to use a discrete Fourier transform (DFT), as is discussed further in appendix D.

The process of signal acquisition whilst traversing  $\mathbf{k}$ -space is an MRI *pulse sequence* and many examples will be discussed in later chapters. In the next section we introduce some very basic examples. It is also interesting to notice that the  $\mathbf{k}$ -space formalism gives us a simple language for describing what a sequence does.

## 1.6 Spatial image formation

In this section we show how the  $\mathbf{k}$ -space idea can be implemented in practice to obtain useful images.

### 1.6.1 Pulse sequences

Pulse sequences are combinations of RF and gradient pulses. The combinations of which serve to create a signal with the desired contrast as well as spatially localise the signal in order to produce an image. In many cases we are able to decouple these two processes. Some form of magnetization ‘preparation’ scheme can be used to create the desired contrast whilst a relatively independent ‘readout’ mechanism can then be used to perform the spatial encoding of this prepared signal. Examples of signal preparation are discussed in chapter 5.

Spatial encoding primarily uses magnetic field gradients, with the  $\mathbf{k}$ -space formalism being often used to describe this process. The objective is to fill  $\mathbf{k}$ -space with acquired data points. The spin warp method fills  $\mathbf{k}$ -space in a Cartesian or raster-style, one line of data points at a time. The signal is acquired, i.e. digitized, in the presence of a constant magnetic field gradient, known as the frequency encoding gradient (FE), with each sample point placed consecutively along the line. The other lines that make up the 2D array are offset from each other by an orthogonal gradient, known as the phase encoding gradient (PE), that applies a warp or twist to the magnetization prior to the frequency encoding gradient. Once the full 2D  $\mathbf{k}$ -space array is acquired, image reconstruction simply involves the application of a standard 2D inverse Fourier transform. Data are usually acquired as a power of two, or zero-padded to a power of two so that reconstruction is via the fast Fourier transform (FFT).

In MRI it is customary to use a Cartesian coordinate system with the FE direction as the  $x$ -axis and the orthogonal PE direction as the  $y$ -axis. A slice select gradient (SS), discussed below, is usually used to define the position and thickness of the slice along the image  $z$ -axis. Note that the image coordinate system can (and usually is) rotated with respect to the system coordinate system by using linear combinations of the three available gradients. This is clinically useful as slices can be oriented favourably with respect to important anatomical features. The scanner coordinate system having the  $z$ -axis parallel to  $\mathbf{B}_0$  is sometimes referred to as the physical ( $x, y, z$ ) and the gradient defined system as the logical (FE,PE,SS).

It is, of course, possible to fill  $k$ -space using different trajectories, such as radial lines or spirals—these methods are discussed in chapter 4.

### 1.6.2 Slice select

At any given position within an FOV the proton spins have only two measurable parameters, frequency and phase; together these can give positional information in a 2D plane—thus a third piece of information is needed for full 3D imaging. In practice the extra information is obtained using a slice select (SS) gradient parallel to the image  $z$ -axis applied simultaneously with the excitation RF pulse. The effect of this is that only spins in a narrow range of  $z$ -values are excited and hence the subsequent signals come from only that slice within the 3D volume. Ideally the selected slice should have a finite thickness with a relatively sharp profile. For this reason, the RF pulse amplitude is modulated by a sinc function, producing a top-hat distribution in frequency. The topic of RF pulse design is discussed further in chapter 3. Effectively the slice select gradient determines the image  $z$  coordinate and thickness of the slice.

### 1.6.3 Phase encode

After the slice selection, a  $y$ -gradient pulse is applied for a short period of time  $\Delta t$ . The effect of this is to make the phase of the spins in the selected slice a function of  $y$ . Thus, using equation (1.14) we see that the phase encode gradient pulse sets  $k_y = G_y \Delta t$  if  $k_y$  was zero, or it sets  $k_y = k_y + G_y \Delta t$  if  $k_y$  was non-zero.

### 1.6.4 Frequency encode

The frequency encode gradient is applied in the  $x$ -direction during signal acquisition at the time of the spin echo. An additional  $x$ -gradient pulse is also needed before this pulse so that together the dephasing caused by the frequency encode gradient itself is cancelled at the time of the spin echo. Typically, the echo signal is digitized into 256 samples. Effectively, data acquisition in the presence of the frequency encode gradient produces a set of  $S(\mathbf{k})$  values with the required range of  $k_x$  values at a particular fixed  $k_y$ .

### 1.6.5 Rewind and repeat

The above three steps generate the signal for one line in  $k$ -space. These steps are then repeated with different values of the phase encode gradient to generate different lines



of data in  $k$ -space. Prior to this it may be necessary to apply additional  $x$  and/or  $y$  gradients to return the phase of the spins back to some defined starting place in  $k$ -space. Typically, 128–256 phase encode steps are used. The time interval between repetitions is known as TR, and has an important effect on image contrast and the total time taken for the scan. Clinically useful MRI sequences use a variety of methods reduce to overall acquisition time of a sequence while also delivering the required contrast. This accounts for much of the complexity of the real sequences described in chapter 4.

The processes described in section 1.6 are shown here as *pulse sequence diagrams*, in figure 1.12 for the spin echo case and in figure 1.13 for the equivalent gradient echo case. The sequences shown here provide a basis for the more complicated practical clinical sequences discussed in later chapters.

The sequences shown in figures 1.12 and 1.13 have a negative  $G_z$  pulse immediately after the positive slice selection pulse, this is necessary to rewind the dephasing caused by the application of the slice select, i.e. the first,  $G_z$  pulse. In principle, a similar rewinding of the  $G_y$  and  $G_x$  pulses might be necessary. However, in this case we are assuming TR is sufficiently long for transverse magnetization to

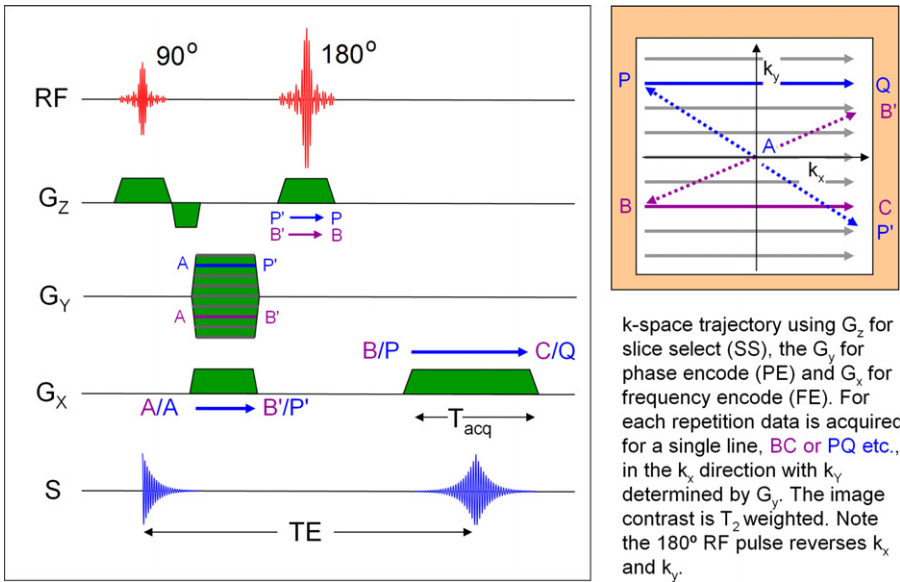


**Figure 1.12.** Basic MRI spin echo sequence with  $z$ -gradient for slice selection and  $x$ - and  $y$ -gradients applied prior to readout to select starting point ( $A \rightarrow B$ , or  $A \rightarrow B$  etc) in  $k$ -space. A second  $x$ -gradient having the same polarity is then applied to readout the  $k$ -space line ( $B \rightarrow C$ , or  $P \rightarrow Q$  etc). The delay between repetitions is known as TR; if TR is long (typically 3–5 times the largest  $T_1$  of the sample), the image is  $T_2$  or PD weighted depending on the echo time. The two  $x$ -gradient pulses have cancelling dephasing and rephasing effects because of the  $180^\circ$  RF pulse that occurs between these pulses. Note the time to echo, TE is exactly twice the time interval between the two RF pulses since the rephasing time after the  $180^\circ$  pulse is equal to the dephasing time between the two pulses. Signal is acquired over a time  $T_{acq}$  during the spin echo. The RF pulses are modulated by a sinc function in order to excite a slice of known thickness.

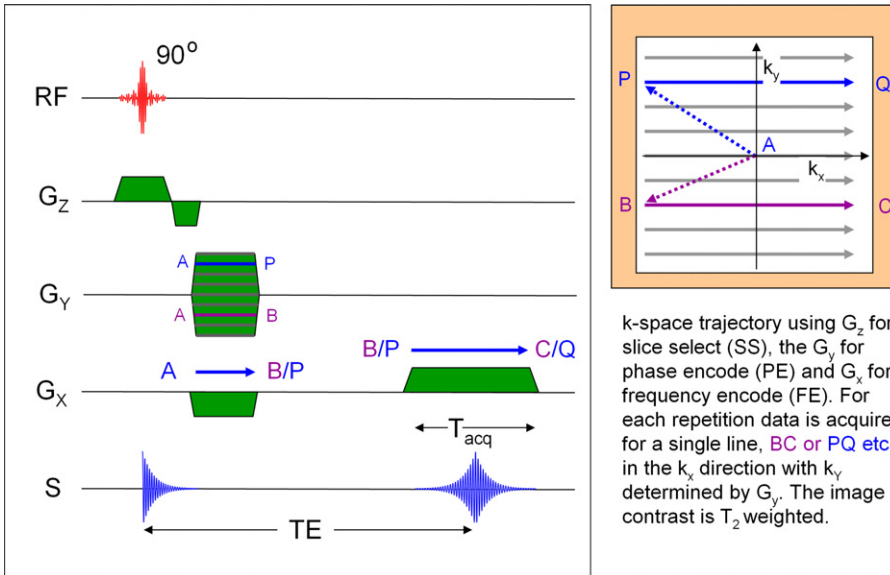


**Figure 1.13.** Basic MRI gradient-echo sequence. It is similar to the SE sequence in figure 1.12 except that the first RF pulse has a tip angle  $\alpha$  which is often less than  $90^\circ$ , the second RF pulse is not required and the first  $G_x$  pulse has reversed polarity. Rephasing to produce the spin echo is now caused solely by the two  $x$ -gradient pulses.

decay to zero before the next  $90^\circ$  RF pulse, so that the  $k$ -space trajectory always starts at  $k_x = k_y = 0$ .

## 1.7 Conclusion

In this chapter we have introduced the basic physical ideas underlying MRI. The next two chapters concentrate on the technical challenges involved in actually creating a reliably performing scanner. In chapter 4 we return to the subject of pulse sequences and in chapter 5 give examples of clinical sequences in action.

The five appendices contain the necessary mathematical details that underpin the whole subject.

## References

- Bloch F 1946 Nuclear induction *Phys. Rev.* **70** 460–74
- Bloch F *et al* 1946 The nuclear induction experiment *Phys. Rev.* **70** 474–85
- Bloembergen N *et al* 1948 Relaxation effects in nuclear magnetic resonance absorption *Phys. Rev.* **73** 679–712
- Carr H Y and Purcell E M 1954 Effects of diffusion on free precession in nuclear magnetic resonance experiments *Phys. Rev.* **94** 630
- Damadian R 1971 Tumor detection by magnetic resonance *Science* **171** 1151–3
- Damadian R 1974 Apparatus and Method for Detecting Cancer in Tissue. US Patent and Trademark Office. U.S. Patent No. 3,789,832.

- de Bazelaire C M *et al* 2004 MR imaging relaxation times of abdominal and pelvic tissues measured *in vivo* at 3.0 T: preliminary results I *Radiology* **230** 652–9
- Dirac P A M 1928a The quantum theory of the electron *Proc. R. Soc. A* **117** 610–24
- Dirac P A M 1928b The quantum theory of the electron - Part II *Proc. R. Soc. A* **118** 351–61
- Edelstein W A *et al* 1980 Spin warp NMR imaging and applications to human whole-body imaging *Phys. Med. Biol.* **25** 751–6
- Ernst R R and Anderson W A 1966 Application of Fourier transform spectroscopy to magnetic resonance *Rev. Sci. Instrum.* **37** 93–102
- Gerlach W and Stern O 1922a The experimental evidence of direction quantization in the magnetic field *Zeitschrift Fur Physik* **9** 349–52
- Gerlach W and Stern O 1922b The magnetic moment of silver atoms *Zeitschrift Fur Physik* **9** 353–5
- Hahn E L 1949 An accurate nuclear magnetic resonance method for measuring spin-lattice relaxation times *Phys. Rev.* **76** 145
- Hahn E L 1950 Spin echoes *Phys. Rev.* **80** 580–94
- Kittel C 2005 *Introduction to Solid State Physics* (New York: Wiley)
- Kunzler J E *et al* 1961 Superconductivity in Nb<sub>3</sub>Sn at high current density in a magnetic field of 88 Kgauss *Phys. Rev. Lett.* **6** 89–91
- Lauterbur P C 1973 Image formation by induced local interactions—examples employing nuclear magnetic resonance *Nature* **242** 190–1
- Levitt M H 2008 *Spin Dynamics: Basics of Nuclear Magnetic Resonance*. (New York: Wiley)
- Liang Z-P and Lauterbur P C 2000 *Principles of Magnetic Resonance Imaging* (Bellingham, WA: SPIE Optical Engineering Press)
- Mansfield P 1977 Multi-planar image-formation using NMR spin echoes *J. Phys. C: Solid State Phys.* **10** L55–L58
- McRobbie D W *et al* 2007 *MRI from Picture to Proton* (Cambridge: Cambridge University Press)
- Meiboom S 1980 Citation classic—modified spin-echo method for measuring nuclear-relaxation times *Curr. Contents/Engineering Technol. Appl. Sci.* **38** 16–16
- Meiboom S and Gill D 1958 Modified spin-echo method for measuring nuclear relaxation times *Rev. Sci. Instrum.* **29** 688–91
- Onnes H K 1911 Further experiments with liquid helium D—on the change of the electrical resistance of pure metals at very low temperatures, etc V the disappearance of the resistance of mercury *Proc. of the Koninklijke Akademie Van Wetenschappen Te Amsterdam* **14** 113–15
- Purcell E M *et al* 1946 Resonance absorption by nuclear magnetic moments in a solid *Phys. Rev.* **69** 37–8
- Pyykko P 2000 Perspective on Norman Ramsey’s theories of NMR chemical shifts and nuclear spin-spin coupling—*Phys. Rev.* **77** 567 (1950) to *Phys. Rev.* **91** 303 (1953) *Theor. Chem. Acc.* **103** 214–16
- Rabi I I 1937 Space quantization in a rotating magnetic field *Phys. Rev.* **51** 0652–4
- Rooney W D *et al* 2007 Magnetic field and tissue dependencies of human brain longitudinal (H<sub>2</sub>O)-H-1 relaxation *Magn. Reson. Med.* **57** 308–18
- Schmitt P *et al* 2004 Inversion recovery TrueFISP: quantification of T(1), T(2), and spin density *Magn. Reson. Med.* **51** 661–7
- Stanisz G J *et al* 2005 T1, T2 relaxation and magnetization transfer in tissue at 3T *Magn. Reson. Med.* **54** 507–12

- Tofts P S 1997 Modeling tracer kinetics in dynamic Gd-Dtpa MR imaging *J. Magn. Reson. Imag.* [7](#) 91–101
- Tofts P S 2003 *PD: Proton Density of Tissue Water. Quantitative MRI of the Brain* (Chichester: Wiley) pp 83–109
- Wyss M *et al* 2013 Relaxation parameter mapping adapted for 7T and validation against optimized single voxel MRS. *Proc. of the 21st Annual Scientific Meeting of ISMRM* (Salt Lake City, USA)